Material Removal Rate Control for a Teleoperated Robotic Sander

Cameron Devine

A thesis
submitted in partial fulfillment of the
requirements for the degree of

Master of Science in Mechanical Engineering

University of Washington

2018

Committee:

Joseph Garbini, Chair

Santosh Devasia

Lance McCann

Program Authorized to Offer Degree:
Mechanical Engineering

University of Washington

Abstract

Material Removal Rate Control for a Teleoperated Robotic Sander

Cameron Devine

Chair of the Supervisory Committee:
Professor Joseph Garbini
Mechanical Engineering

During the manufacture of aircraft interior panels, the surfaces must be sanded before paint or decorative laminates can be applied. Defects in the panel are fixed by applying Bondo, and then sanding the surface until it is smooth and flat. This work is currently being performed by hand, but there is a desire to make this work more ergonomic through automation and other tools. In most cases automated sanding is performed with a constant normal force, however this can lead to uneven sanding. To address this issue, a model of the sanding material removal rate is derived and experimental parameters are estimated. Furthermore, this model can be used to determine the normal force required to maintain a consistent material removal rate. A controller is then designed, implemented, and tested to maintain this consistent material removal rate.

DEDICATION

To George Hoke, my grandfather, who showed me the joys of learning and discovery, the satisfaction of building, and the reward of years of hard work.

ACKNOWLEDGMENTS

My mother, who taught me everything I needed for my postsecondary education.

My father, who helped me build and experiment.

Rico Picone, who encouraged me to continue my college education.

Professor Garbini, who guided me through this program.

Those in the BARC lab, who aided me with my research.

Tamara, whose unconditional love and support aided every chapter of this work.

Without you, I would not be here today.

TABLE OF CONTENTS

LIST OF FIGURES

Chapter 1

INTRODUCTION

In Boeing's Interiors Responsibility Center (IRC), aircraft interior panels are manufactured. These panels have a crushed core construction, consisting of three composite layers: inner and outer fiberglass layers, and a fiberglass honeycomb interior structure. Various part geometries are created by compressing the panel in a mold while it cures to set the part geometry. Next paint or decorative laminates are applied. Prior to this operation, the panel must be sanded to increase adhesion. Furthermore, any defects are removed by applying Bondo, then sanded to match the original contour of the surface. Although this process is sufficient for producing quality aircraft parts, there are several ergonomic concerns for those who perform this sanding.

The majority of sanding in the IRC is performed using a hand held, air powered, random orbit sander. Due to the vibration transmitted to the hand when operating the sander, Vibration White Finger is known to occur, which causes affected fingers to lose blood flow, turn white, and become numb. For horizontal flat panels, tools exist, and are in development, which limit the vibrations imparted on the operator.

Shoulder injuries are also common due to the pressure required to effectively sand the surface. This issue is aggravated when the center of a large panel needs to be sanded, where the added reach puts considerable strain on the shoulder. Weighted sanders can be used to alleviate some of this risk.

Although sanding is performed in a dust booth which constantly pulls in clean air, it is still likely that some dust is inhaled. While the effect of this dust on the respiratory system is not entirely known, improvements which remove the operator from the dust filled

environment would be beneficial.

In some cases, standard industrial robots are used for high volume parts. However, most parts are not produced at a high enough volume for this approach to be feasible. Furthermore, these robots typically use a constant force for sanding which can cause uneven sanding to occur. To address these concerns a robot was designed in Chapter 2. A model for the material removal rate of the sanding process was derived in Chapter 3 and the experimental constant for the model estimated in Chapter 4. A controller was then designed, implemented, and tested in Chapter 6 to maintain a constant material removal rate.

Chapter 2

ROBOT DESIGN

To alleviate the ergonomic concerns in Chapter 1, a robot with the following traits was designed. The robot will wield the sander, thereby eliminating the vibrational and pressure loads on the operator. A wireless XBox Controller allows the operator to dictate the path of the sander and other necessary information either close to the part, or away from the dust generated.

2.1 Robot Description

This robot consists of a three axis gantry and a four degree of freedom robotic arm built with series elastic actuators. At the end of the arm is a 5in random orbit sander. Between the sander and the robotic arm is a 6 axis force/torque sensor, used to detect the contact loads on the sander. Finally, a LIDAR sensor is mounted on the gantry to allow collection of a point cloud representation of the workpiece. This robot is shown in Fig. 2.2.

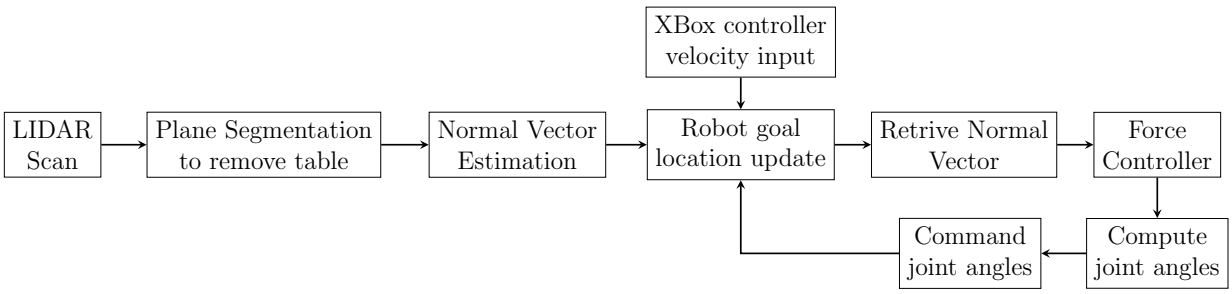

Figure 2.1: A flowchart showing the steps performed by the controller during the operation of the sanding robot.

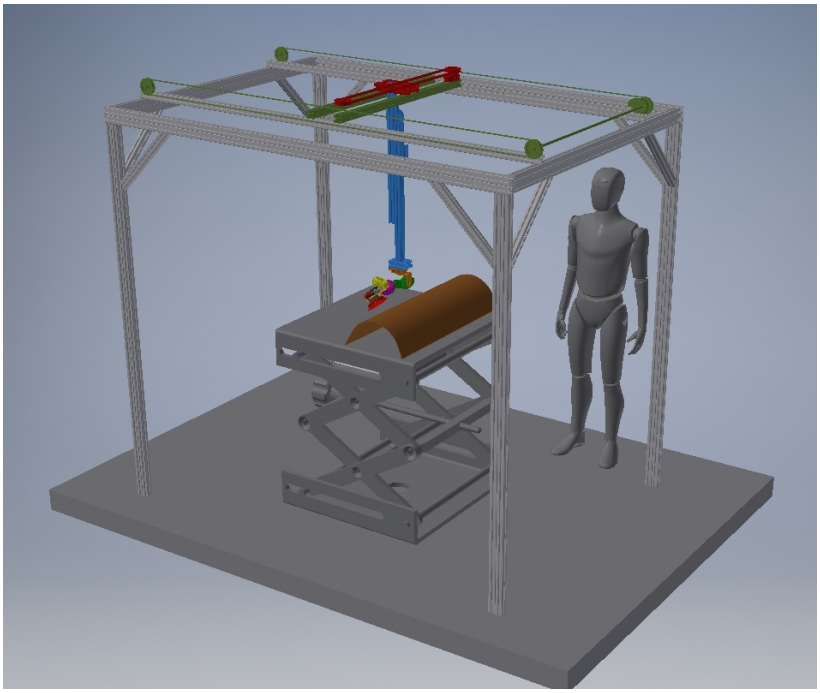

Figure 2.2: The robot design consisting of a three axis gantry, a four degree of freedom robot arm, a sander, and a six axis force torque sensor.

2.2 Operational Process

The robot operates in two stages, first the LIDAR scan of the part is performed, then the operator is given control of the sander path.

2.2.1 LIDAR Scan

The LIDAR sensor used on the robot measures the distance from the spinning head to a single point, scanning a line across the workpiece as the head spins. To scan the entire part, the gantry is moved along its entire length of travel. Once the scan is complete the RANSAC method[1] inside PCL[9] was used to remove the points near the plane assumed to be the table. Finally the normal vectors of the part surface were estimated using a linear least squares approach[8] in PCL[9].

2.2.2 Operator Control

Once the point cloud has been created the operator is given control of the sander path velocity using the XBox controller. Using the commanded location the normal vector is retrieved from the point cloud. To control the contact force of the sander, the goal location of the robot is modified to press further into the workpiece to apply more force, or retract from the workpiece to apply less. This modifies the preload on the springs in the series elastic actuators. With the goal location and normal vector, the desired robot pose is known. Inverse kinematics is then used to calculate[4] the desired robot joint angles. The robot joints are then commanded to these angles, and the loop is repeated. This series of steps is shown in Fig. 2.1.

Chapter 3

SANDING MATERIAL REMOVAL RATE MODEL

With the general goal of controlling material removal rate in real time, a formula for material removal rate per unit area must be found. A second equation is also derived which takes into account the linear motion of the sander.

3.1 Fundamental Equations

The basis of the material removal rate equations derived here is the Preston equation[6],

$$\dot{h} = k_p p v, \tag{3.1}$$

where $\dot{h}$ is the volume of material removed per unit area per unit time, k_p is an experimentally determined constant, p is the sanding pressure, and v is the sanding velocity. As the sander uses a orbital pattern the velocity of a given point on the sander is a function of radius and time[5],

$$\Delta v(r,t) = \sqrt{r^2\omega_p^2 + E^2\omega_m^2 + 2rE\omega_p\omega_m \cos((\omega_p - \omega_m)t)}, \tag{3.2}$$

where r is the radius of a point on the sanding pad, E is the sander orbit eccentricity, ω_p is the rotational velocity of the sanding pad relative to the sander body, ω_m is the rotational speed of the orbit motion, and t is time.

3.2 Velocity Simplification

In previous experiments[5] $\omega_m = 5946$ rpm and $\omega_p = 211$ rpm. Because $\omega_p << \omega_m$, ω_p can be considered negligible. This allows Eq. 3.2 to be simplified to,

$$\Delta v = E\omega_m. \tag{3.3}$$

3.3 Average Linear Velocity

Eq. 3.2 was designed for an orbital sander on a single point trajectory. Therefore some modification was necessary to include linear velocity. Given a linear velocity v_l in the x direction, the linear velocities of the orbital motion in the x and y directions can be found as,

$$\begin{aligned} v_{rx} &= E\omega_m \cos(\omega_m t) \\ v_{ry} &= E\omega_m \sin(\omega_m t). \end{aligned} \tag{3.4}$$

This allows the following equations to be written,

$$\begin{aligned} v_x &= v_l + E\omega_m \cos(\omega_m t) \\ v_y &= E\omega_m \sin(\omega_m t). \end{aligned} \tag{3.5}$$

Using these equations the linear velocity as a function of time can be written as,

$$v(t) = \sqrt{(v_l + E\omega_m \cos(\omega_m t))^2 + (E\omega_m \sin(\omega_m t))^2}. \tag{3.6}$$

This equation can now be integrated around a full revolution to find the mean velocity,

$$v(\omega_m, v_l) = \frac{\omega_m}{2\pi} \int_0^{\frac{2\pi}{\omega_m}} \sqrt{(v_l + E\omega_m \cos(\omega_m t))^2 + (E\omega_m \sin(\omega_m t))^2}\, dt. \tag{3.7}$$

The following Mathematica code can be used to evaluate the integral:

```
vr = omega r;
vrx = vr Cos[omega t];
vry = vr Sin[omega t];
vx = vrx + vl;
vy = vry;
v = Sqrt[vx^2 + vy^2];
tf = 2 Pi / omega;
vavg = Integrate[v, {t, 0, tf},
    Assumptions -> {Element[r, Reals], Element[omega, Reals],
      Element[vl, Reals], vr^2 != vl^2 }] / tf
```

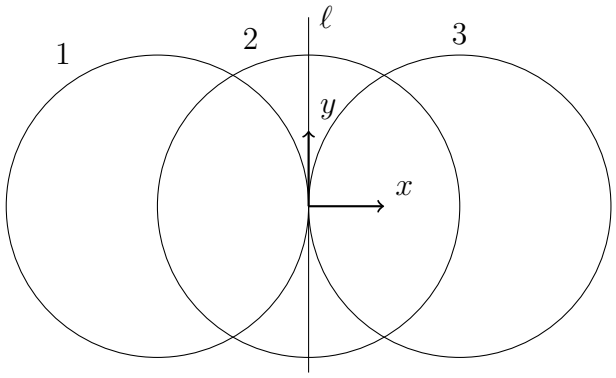

Figure 3.1: Schematic of a sander (circles 1, 2, and 3) sanding over a line ℓ.

This produces the output,

$$v(\omega_m, v_l) = \frac{|v_l - \omega_m E|\, E(-\frac{4\omega_m E v_l}{(v_l-\omega_m E)^2}) + |\omega_m E + v_l|\, E(\frac{4\omega_m E v_l}{(\omega_m E+v_l)^2})}{\pi}, \tag{3.8}$$

where $E(m)$ is the Complete Elliptic Integral of the Second kind. This equation can be combined with Eq. 3.1 to find the material removal rate of the sander,

$$\dot{h} = k_p p v(\omega_m, v_l). \tag{3.9}$$

3.4 Sanding Duration of a Moving Sander

Although Eq. 3.9 is useful, there are times where the average material removed in a given area, taking into account the sander linear velocity, is more representative of the work being performed. To create this formula the average material removal rate of the sander moving over a line perpendicular to the direction of motion is calculated. A diagram of this motion can be found in Fig. 3.1. Since the sander is circular the following describes the edge of the sander,

$$R^2 = x^2 + y^2, \tag{3.10}$$

where R is the radius of the sanding pad, and x and y are the coordinates which lie on the edge of the sanding pad. This equation can be rearranged to the following form,

$$x(y) = \sqrt{R^2 - y^2}, \tag{3.11}$$

where $x(y)$ can be interpreted as the distance the sander travels over line ℓ when moving from circle 1 to circle 2 in Fig. 3.1, and y is a coordinate as defined in Fig. 3.1. By dividing this equation by the linear velocity, v_l, the duration of sanding when the sander moves from circle 1 to circle 2 can be found for any point on line ℓ,

$$t(y) = \frac{\sqrt{R^2 - y^2}}{v_l}, \tag{3.12}$$

where t is the duration of sanding at point y as the sander moves from 1 to 2 in Fig. 3.1. To find the sanding duration for a sander moving from 1 to 3, Eq. 3.12 can simply be doubled,

$$t(y) = 2\frac{\sqrt{R^2 - y^2}}{v_l}. \tag{3.13}$$

3.5 Average Sanding Duration of a Moving Sander

In Sec. 3.4 the duration of sanding at a point on a line perpendicular to the direction of travel was found. Given this information the average duration of sanding on this line can be calculated using the following integral,

$$\bar{t} = \frac{1}{Rv_l}\int_{-R}^{R} \sqrt{R^2 - y^2}\, dy, \tag{3.14}$$

where $\bar{t}$ is the average sanding duration. Evaluating this integral the average sanding duration is found to be,

$$\bar{t} = \frac{\pi R}{2v_l}. \tag{3.15}$$

3.6 Material Removed on the Sanding Path

By combining Eqs. 3.1, 3.8, and 3.15, the following equation can be constructed,

$$\begin{aligned} \bar{h} &= \dot{h}\bar{t} \\ &= k_p p v(\omega_m, v_l)\frac{\pi R}{2v_l}, \end{aligned} \tag{3.16}$$

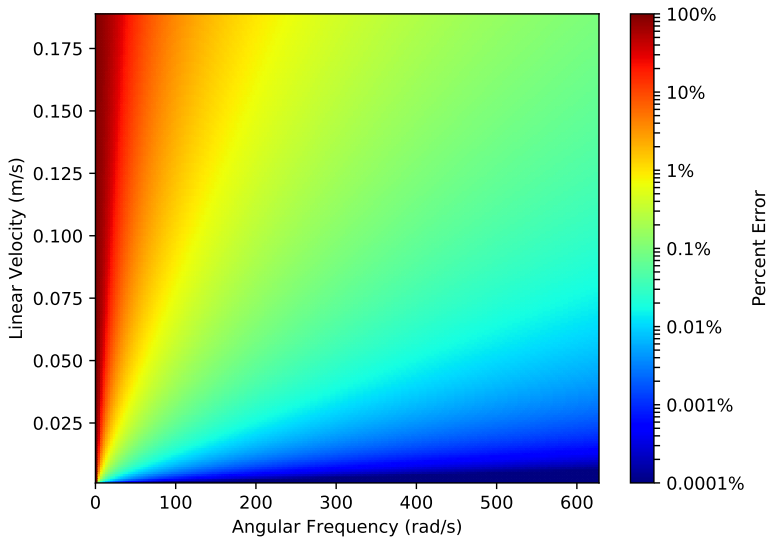

Figure 3.2: The percent error of a simplified average velocity equation (Eq. 3.17) which removes the dependence on the linear velocity versus the full average velocity equation (Eq. 3.8).

where $\bar{h}$ is the material removed per unit area on line ℓ while the sander moves from circle 1 to circle 3 in Fig. 3.1, with linear velocity v_l, orbital velocity ω_m, and pressure p.

3.7 A Simplified Average Velocity Equation

The average velocity equation, Eq. 3.8, is nonlinear and reasonably complex. Because the linear velocities during sanding are much smaller than the orbital velocities of the sander, a simpler linear equation may be reasonably accurate,

$$v = E\omega_m. \tag{3.17}$$

The percent error of the full equation (Eq. 3.8) versus the simplified equation (Eq. 3.17) over the normal range of linear and rotational velocities can be viewed in Fig. 3.2. From this figure it can be seen that under the normal rotational velocity of 600 $\frac{\text{rad}}{\text{s}}$ the error is

between 0 and about 0.1% for velocities up to 0.18 $\frac{\text{m}}{\text{s}}$, the maximum velocity of the robot. As the rotational velocity, in recorded data, rarely dips below 600 $\frac{\text{rad}}{\text{s}}$ the simplified average velocity equation can be used without significant effects to the results. This allows a linear version of Eq. 3.16 to be written,

$$\bar{h} = \frac{\pi k_p p R E \omega_m}{2 v_l}. \tag{3.18}$$

3.8 Material Removal Rate Model Inversion

For control purposes, the inverse of Eq. 3.18 is desired. This equation would be used to determine the necessary pressure to maintain a constant material remove rate. As Eq. 3.18 is linear, this is easily accomplished by solving for p,

$$p = \frac{2 \bar{h} v_l}{\pi k_p E \omega_m R}. \tag{3.19}$$

To find the force required, Eq. 3.19 can simply be multiplied by the contact area of the sander.

Chapter 4

CONSTANT ESTIMATION FOR THE MATERIAL REMOVAL RATE MODEL

Given the model in Chapter 3, the value of k_p must be found. This value was found by sanding three parts at three different forces and three different linear velocities, for a total of nine tests per test article. Given the three test article this is a total of 27 tests. However, five verification tests were also performed, two for each curved part, and one for the single flat part. In total, there are 32 tests to perform. The order of these tests was randomized providing the list in Appendix A. To create a repeatable surface, Bondo was added to the test articles between tests, when needed. This allows each part to be sanded multiple times without needing to be replaced. For each test, the part was sanded using the robot with 120 grit sandpaper. The path of the sander was controlled using the XBox controller to give a pseudo random path. After the tests were complete the data was analyzed to find k_p.

4.1 Material Removal Rate Equation for Constant Equation

For this test, an equation can be derived from Eq. 3.9 which requires data which is easier to collect from the robot,

$$\dot{h} = k_p p v(\omega_m, v_l) \tag{4.1}$$

$$\frac{\dot{V}}{a} = k_p \frac{f}{a} v(\omega_m, v_l) \tag{4.2}$$

$$\dot{V} = k_p f v(\omega_m, v_l) \tag{4.3}$$

$$\frac{\dot{m}}{\rho} = k_p f v(\omega_m, v_l), \tag{4.4}$$

where $\dot{V}$ is the volume of material removed per unit time, a is sander contact area, f is the sanding normal force, and ρ is the density of the material being sanded. To determine the

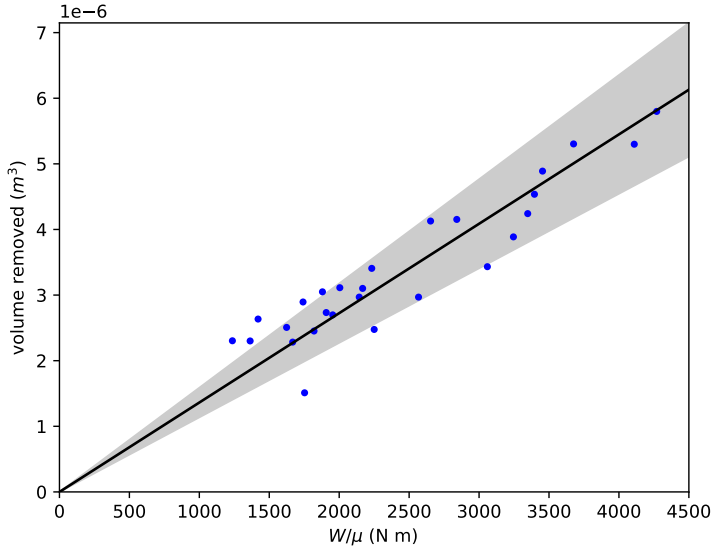

Figure 4.1: Measured volume removed as a function of normalized work done using the 27 training data points plotted with the linear fit and a shaded one standard deviation band.

volume of material removed over the duration of the sanding, this equation can be integrated over time,

$$\Delta V = \frac{\Delta m}{\rho} = \int_0^{t_f} k_p f v(\omega_m, v_l)\, dt, \tag{4.5}$$

where ΔV is the volume of material removed and Δm is the change in mass over the time interval from 0 to t_f, the duration of the sanding.

The work done during this sanding operation is[6],

$$W = \mu \int_0^{t_f} f v(\omega_m, v_l)\, dt, \tag{4.6}$$

where W is the work done, and μ is the average coefficient of friction during sanding. To further simplify Eq. 4.5 the integral of force times velocity can be replaced with $\frac{W}{\mu}$,

$$\frac{\Delta m}{\rho} = k_p \frac{W}{\mu}, \tag{4.7}$$

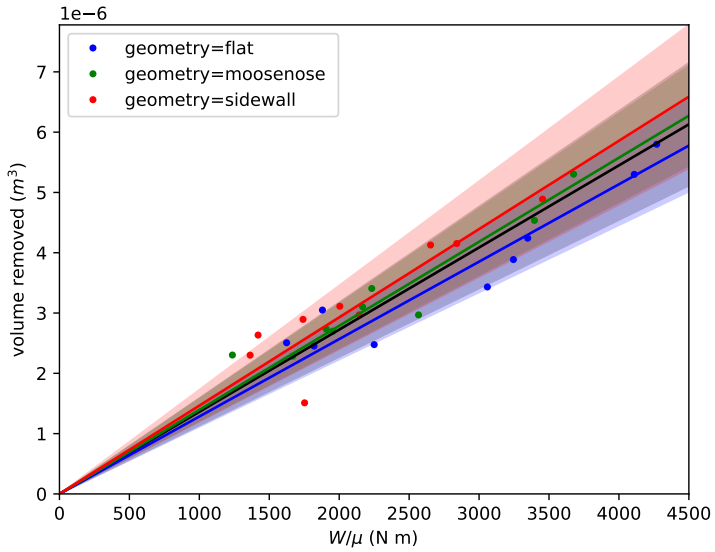

Figure 4.2: Measured volume removed as a function of normalized work done using the 27 training data points displayed with different colors for each test article geometry, plotted with a linear fit and a corresponding shaded one standard deviation band for each panel geometry along with the overall fit.

The value of $\frac{W}{\mu}$ can be found for the time interval from 0 to t_f using,

$$\frac{W}{\mu} = \int_0^{t_f} f v(\omega_m, v_l)\, dt. \tag{4.8}$$

4.2 Required Data for Estimation

To determine the material removal rate, data was collected to enable the use of the equations in Sec. 4.1. For these tests, each article was weighed both before and after sanding. As the density of the Bondo is know to be $\rho = 1.13\ \frac{\text{g}}{\text{cm}^3}$ the volume of material removed can be calculated. During sanding, the following data was collected at an interval of 0.01 seconds for the duration of the sanding.

- Sander Position

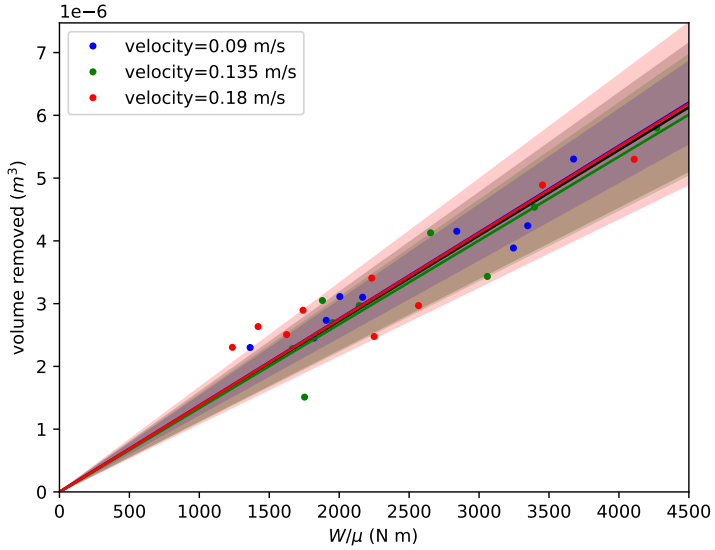

Figure 4.3: Measured volume removed as a function of normalized work done using the 27 training data points displayed with different colors for each linear velocity, plotted with a linear fit and a corresponding shaded one standard deviation band for each velocity along with the overall fit.

- Sander Orbital Velocity
- Sander Normal Force

4.3 Material Removal Rate Data Analysis

Once collected, some filtering was required to clean the recorded data. In the RPM data initial readings were occasionally pinned at 6×10^7 RPMs. This was easily fixed by replacing all values of 6×10^7 with 0. Multiple large spikes were also observed in the data. To remove these spikes, a rolling median filter was used with a window size of 7 samples. This effectively removed all the spikes in the data.

The sander's linear velocity was calculated by numerically differentiating the sander position. The average velocity for Eq. 4.8 was calculated using Eq. 3.8. Finally, Eq. 4.8 was

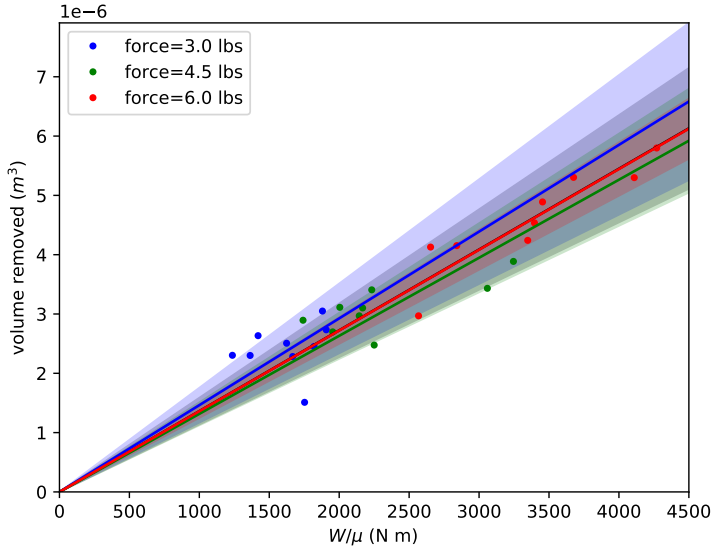

Figure 4.4: Measured volume removed as a function of normalized work done using the 27 training data points displayed with different colors for each force, plotted with a linear fit and a corresponding shaded one standard deviation band for each force along with the overall fit.

used to calculate the work done over the duration of the sanding.

Once the work was calculated, the initial and final mass measurements were used to determine the volume of material removed. This information was used to calculate a linear fit of Eq. 4.7 to estimate k_p.

To find the standard deviation, each data point can be used to calculate its own constant k_p. These constants can be used with the ordinary standard deviation formula giving the standard deviation of the linear fit.

4.4 Material Removal Rate Constant Estimation Test Results

After all data was processed the data was plotted along with the fit, and a shaded one standard deviation band. This data can be seen in Fig. 4.1. Although there is some variation

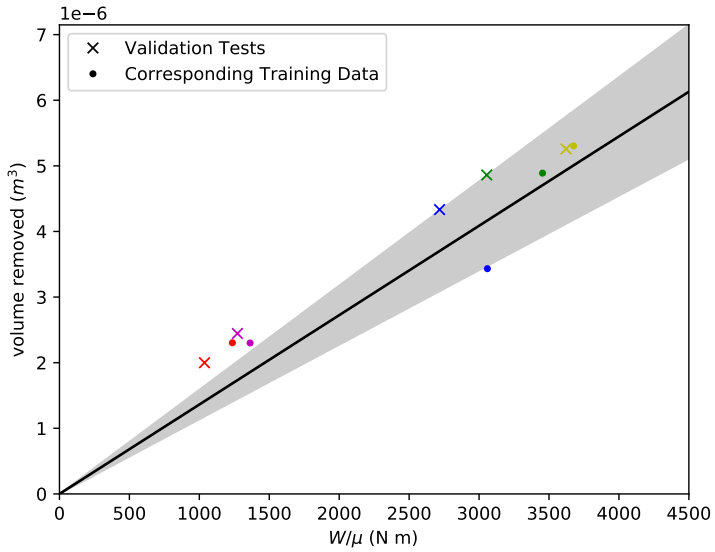

Figure 4.5: Measured volume removed as a function of normalized work done using the five validation data points with their corresponding tests run with the same parameters, along with the overall linear fit and one standard deviation band.

in the data it is linear and consistent.

The data was then plotted in Fig. 4.2 with a different color for each test article. Looking at the points there are some geometries which are consistently higher or lower than others, but the overall linear fit is well within the one standard deviation band of each fit. Overall this is an expected result where the geometry information does not largely impact the result.

When split by velocity, the individual fits are extremely consistent. This can be seen in Fig. 4.3. The consistence between the fits is likely due to the fact that the sander orbital speed dominates Eq. 3.8. Interestingly, the standard deviation is larger for higher velocities.

Looking at the data split by force, the results could be more consistent, but again the individual fits are well within the one standard deviation band of the overall fit. In Fig. 4.4 the tests with higher forces have had more volume removed, and a larger amount of work done, as expected.

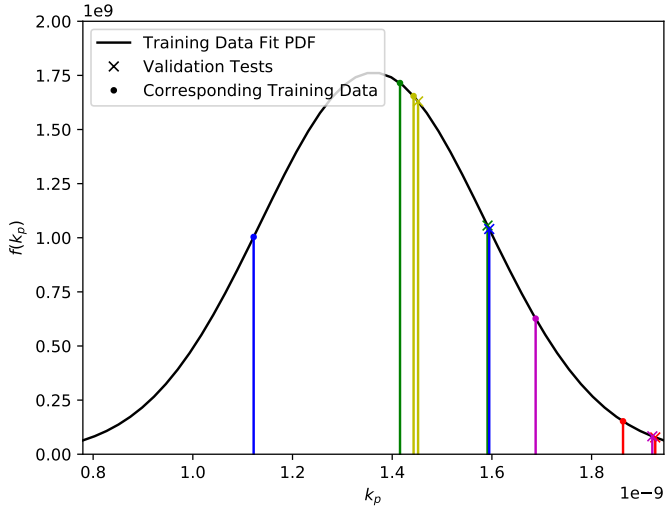

Figure 4.6: The normal probability density function of the estimated material removal rate constant, k_p, with the 5 validation data points and their corresponding tests run with the same parameters.

The final results of this testing are a value of $k_p = 1.362 \times 10^{-9}$ $\frac{\mathrm{m\,s^2}}{\mathrm{kg}}$ and a standard deviation of $\sigma = 2.263 \times 10^{-10}$.

4.5 Material Removal Rate Estimated Constant Validation Results

The validation tests were processed in the same way as the standard training data. These tests were then plotted with the other tests run with the same parameters in Fig. 4.5. In general the validation tests and the corresponding training data are close to each other. However there are two exceptions. In the blue data points the training data and validation test appear on different sides of the one standard deviation band. In the green data points the validation test is much further from the linear fit than its corresponding test.

The same validation data was also plotted on the PDF of the linear fit in Fig. 4.6. This plot shows more clearly the differences between the tests. Of note are the blue data points which are at similar probability on opposite sides of the PDF. Similarly expected are the

green data points which are at extremely different probabilities. More unexpected is the difference in probability of the magenta data points. Due to their proximity to the origin the small distance between the two points produces a large change in slope probability.

Chapter 5

ROBOT SYSTEM IDENTIFICATION

Before controllers can be designed, the dynamics of the system must be measured. These identified systems will be used to simulate the effects of different controllers and aid the design process.

5.1 Robot System Identification

Before a controller can be designed the dynamics of the robot must be measured. To control the normal force for sanding the sander is pressed further into the panel, or pulled away

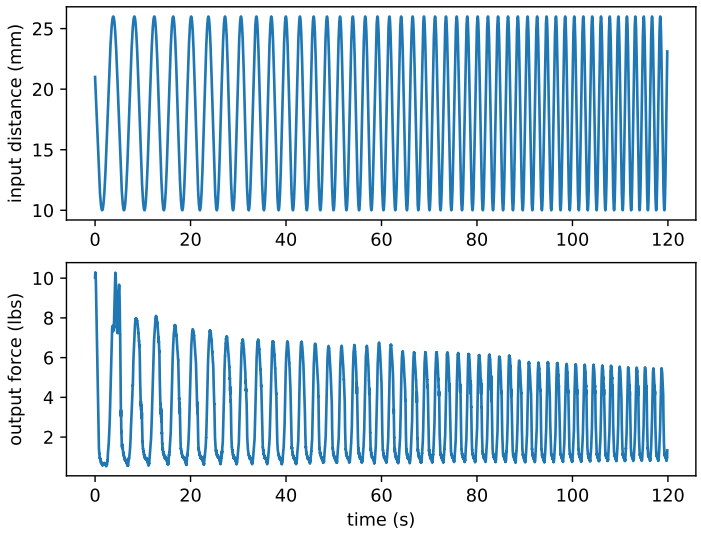

Figure 5.1: The resulting force measured by the pushing the sander a given distance into the workpiece for system identification purposes.

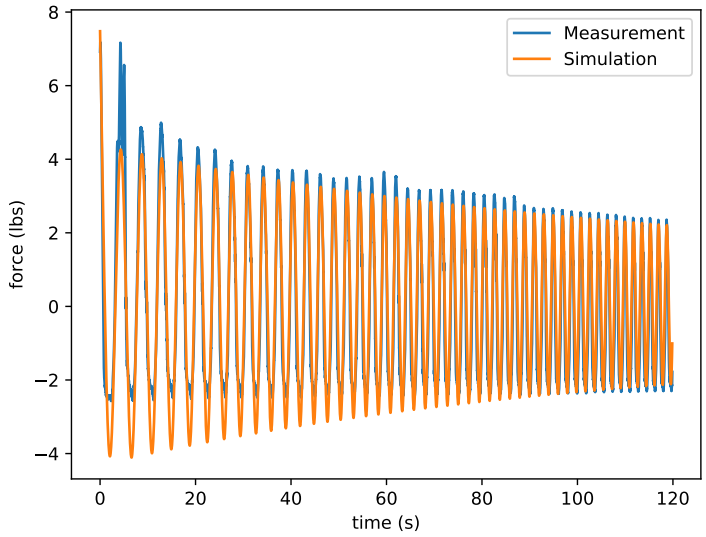

Figure 5.2: The dynamic response of the simulated estimated system model with the response from the physical system.

from the panel. This change in the goal location changes the preload in the series elastic actuators. To find the transfer function of this system, a sinusoidal frequency sweep was used as the input, and the resulting output force was measured. This data is plotted in Fig. 5.1. Before using the ARX[3] method to determine a discrete time transfer function, the input and output data was centered around zero by subtracting the mean. Using the bilinear transformation[2] the resulting discrete time transfer function was converted into a continuous time transfer function. The continuous time system was then simulated with the same frequency sweep input as used to collected the training data. The results of this simulation were then plotted with the collected output data show in Fig. 5.2.

5.2 Sanding Orbit Speed Estimation

To simulate the entire sanding system, a model for sander orbital speed must be created. Previously collected force and RPM data was plotted together in Fig. 5.3 showing a propor-

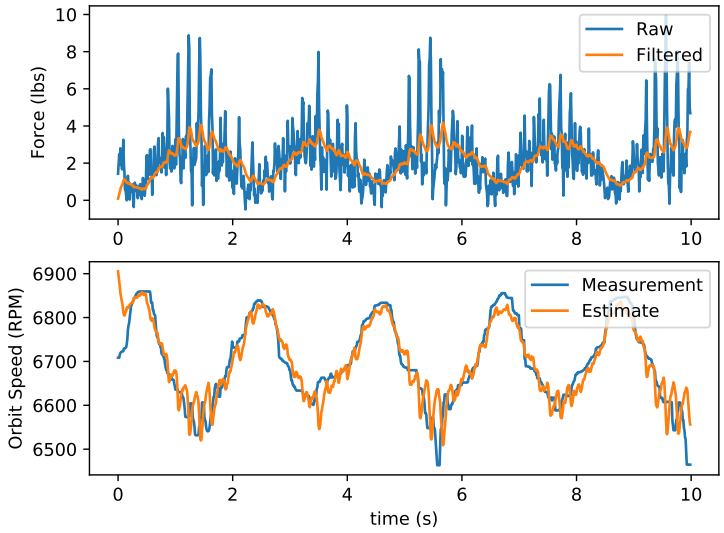

Figure 5.3: Measured and filtered normal force data from the robot with RPM data measured by the robot, and estimated from the normal force.

tional relationship between the two quantities. However, noise in the force data, and spikes in the RPM data were present, so a low-pass filter with a time constant of 0.15 was used to smooth the force data, and a median filter with a window size of 31 samples was used to remove spikes in the RPM data. A linear fit of the filtered data was used to find the relationship between force and RPM in Fig. 5.4. Using this fit, the measured and estimated RPM is plotted in Fig. 5.3.

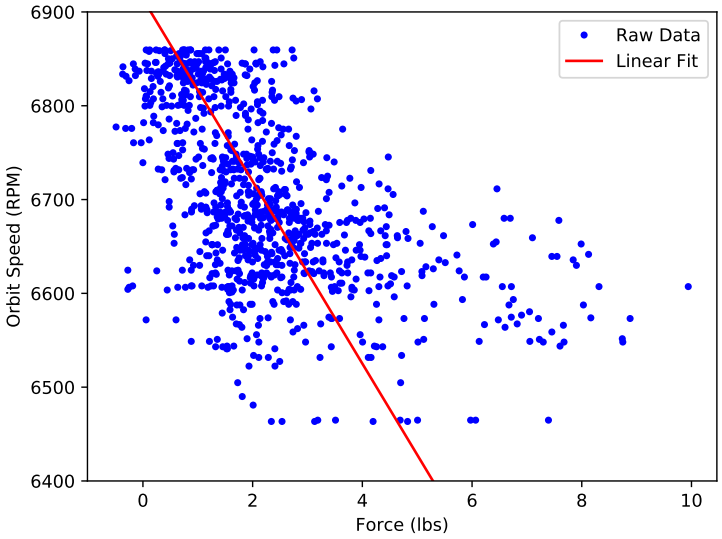

Figure 5.4: The median fitlered measured RPM versus the lowpass filtered measured normal force and a linear fit to estimate the sander RPM from force data.

Chapter 6

MATERIAL REMOVAL RATE CONTROL

With a model derived and the constant estimated, a controller can now be designed which provides a constant material removal rate as defined in Eq. 3.16. Once designed, this controller was simulated to determine if the performance was satisfactory.

6.1 Robot Force Controller

To control the sanding material removal rate, a force controller was used to maintain a specified force necessary for the desired material removal rate. The first step in designing

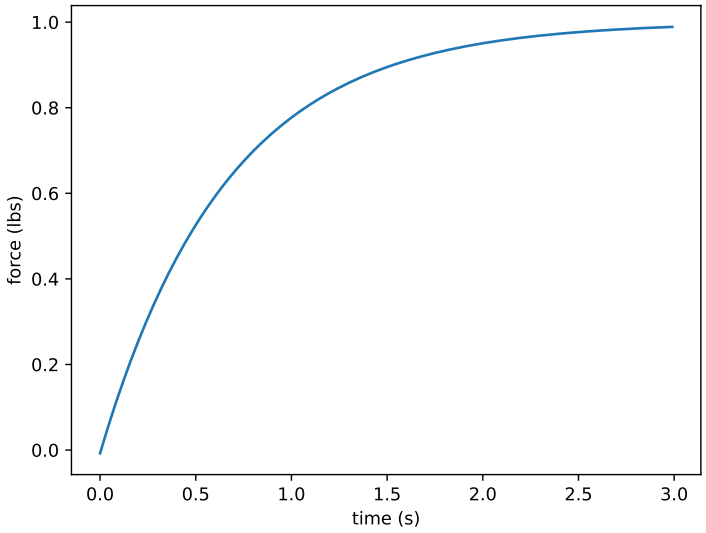

Figure 6.1: The step response of the control system in Fig. 6.2 with only feed forward gain.

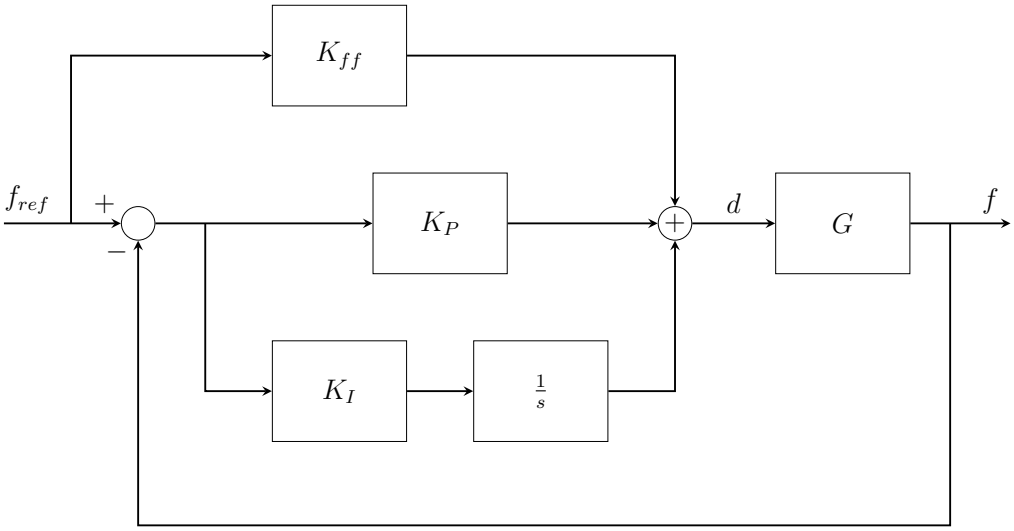

Figure 6.2: The force controller block diagram with desired force input (f_{ref}), controller output of the distance to push into the workpiece (d), the plant (G) identified in Chapter 5, and the resulting force (f).

this controller was to determine the feed forward gain,

$$\frac{1}{\text{dcgain}(G)} = K_{ff}, \tag{6.1}$$

where G is the transfer function of the plant as found in Sec. 5.1. Using only feed forward gain the system was simulated and the results plotted in Fig. 6.1. While the system is stable, and does reach the correct value, the settling time is much slower than desired. To counteract the problem a closed loop proportional gain was added, as shown in Fig. 6.2. To determine the proportional gain, the theoretical closed loop settling time was plotted versus the proportional gain in Fig. 6.3. The overshoot was estimated to be zero because all poles are on the real axis. In order to achieve a settling time of about a quarter second, a proportional gain $K_P = 18$ was selected. The closed loop system was then simulated with feed forward gain and a proportional controller. As can be seen in Fig. 6.4, the simulated settling time is indeed about a quarter of a second.

Naturally, steady state errors occur in real world applications. To effectively manage

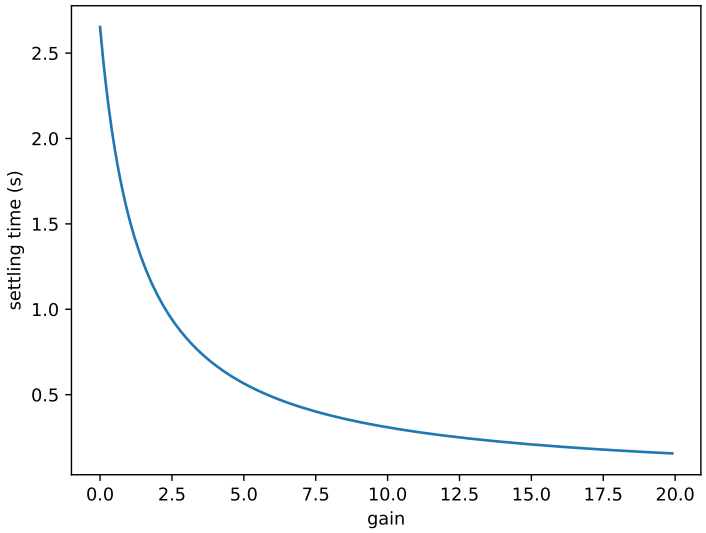

Figure 6.3: The theoretical closed loop settling time with respect to the proportional gain of the control system in Fig. 6.2.

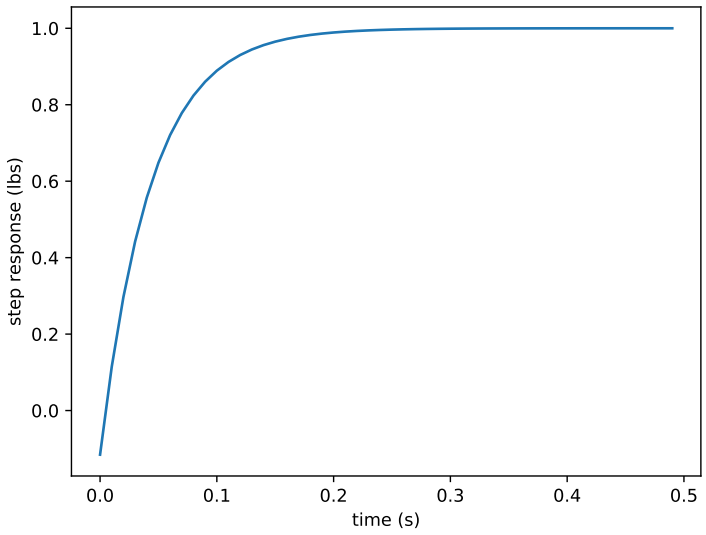

Figure 6.4: The closed loop step response of the control system in Fig. 6.2 with proportional and feed forward gains.

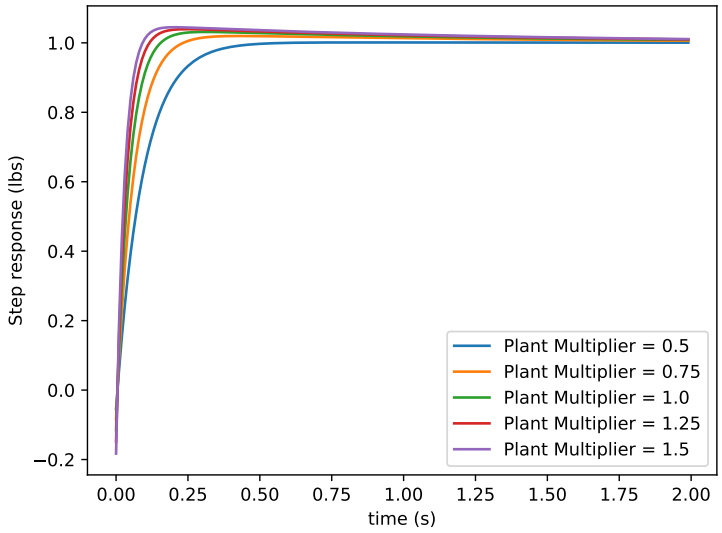

Figure 6.5: The step response of the full controller show in Fig. 6.2 with several plants, each multiplied by a different constant to show the effects of the integral controller.

this issue, integral gain was added to the system. An integral gain $K_I = 15$ was chosen to effectively remove settling time. The final controller was then simulated with multiple plants, each multiplied by a different constant. This shows the effects of the integral gain on the system to be evaluated. The step response of the full controller is shown in Fig. 6.5.

Overall, this control system works very well with the worst case system having a settling time of about one second, and in most cases close to a quarter of a second. Steady state errors are also corrected reasonably quickly, in a maximum of about a second and a half. Although some overshoot is present, it is not excessive.

This overshoot is not predicted when selecting the proportional and integral gains because the resulting system is fourth order. The equation used to calculate the settling time and percent overshoot is based on a second order assumption for all pole pairs[7]. Because the system is fourth order, the dynamics of the system may not completely match the second order approximation used in these calculations.

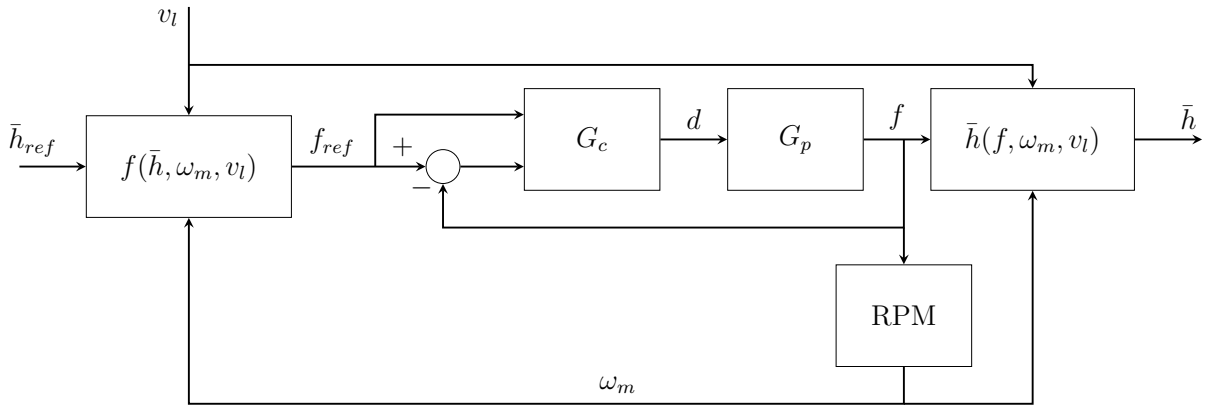

Figure 6.6: A block diagram of the full system to be simulated with the controller (G_c) designed in Sec. 6.1, the plant (G_p) identified in Chapter 5, and RPM model identified in Chapter 5. The inputs to the simulation are the desired material removal rate ($\bar{h}_{ref}$), and the time varying linear sander velocity (v_l). The output is the material removal rate ($\bar{h}$).

6.2 Material Removal Rate Controller Simulation

To ensure the designed force controller performs adequately, the entire system was simulated. The system simulated is shown in Fig. 6.6. For this simulation a constant desired material removal rate was defined, along with a sinusoidal position input as shown in Fig. 6.7. Informing this simulation is the model of the sanding robot found in Sec. 5.1, the force controller designed in Sec. 6.1, and the estimate of sander orbit speed determined in Sec. 5.2. The resulting controlled force, desired force, and estimated sander orbital velocity are shown in Fig. 6.7. The desired and resulting material removal rate is shown in Fig. 6.8

Although there are some large spikes in the simulated material removal rate, these are not as terrible as they may appear. Because the linear velocity, v_l, is in the denominator in Eq. 3.18, when the linear velocity is low any error in the force is magnified. In Fig. 6.7 the force error can be seen to be reasonable for the full period of the sanding. Since the force is proportional to the material removal rate defined in Eq. 3.1, the error between the desired

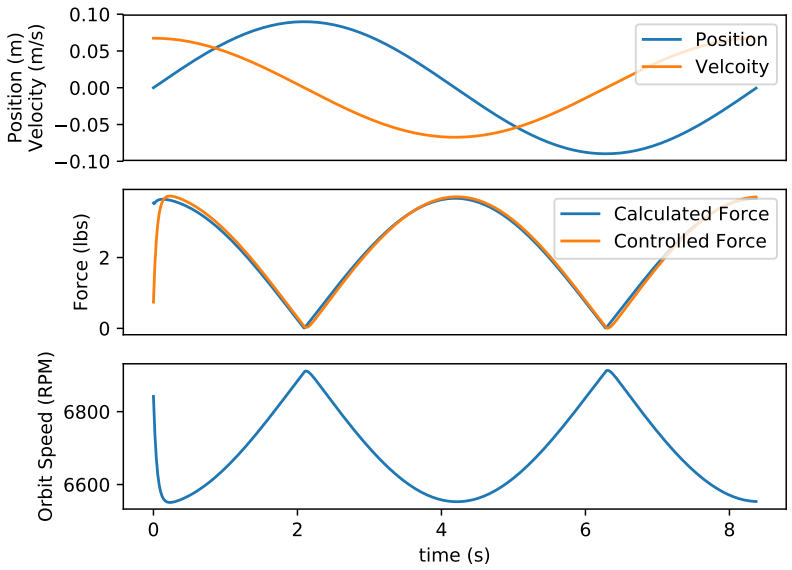

Figure 6.7: Material removal rate controller simulation position, velocity, commanded force, controlled force, and sander orbit speed versus time.

and actual amount of material removed at each location is reasonably small.

6.3 Sander Normalization Control

As the robot was built with series elastic actuators, deflection occurs when forces are exerted on the sander. Because of the geometry of the robot arm, this deflection often causes the sander to lose normality to the surface. To deal with this issue an integral controller was initially used to drive the measured torque at the sander to zero. This technique worked well for a constant force, however the response time was too slow for the rapidly changing force dictated with a constant material removal rate controller. To fix this issue, the sander was manually normalized at a range of forces applied. The collected data is shown in Fig. 6.9 along with a linear fit of this data. This linear fit was then used to normalize the sander at any desired normal force. The new controller was tested and produced equal, if not better, normalization, without the time needed for the integral controller to reach steady state.

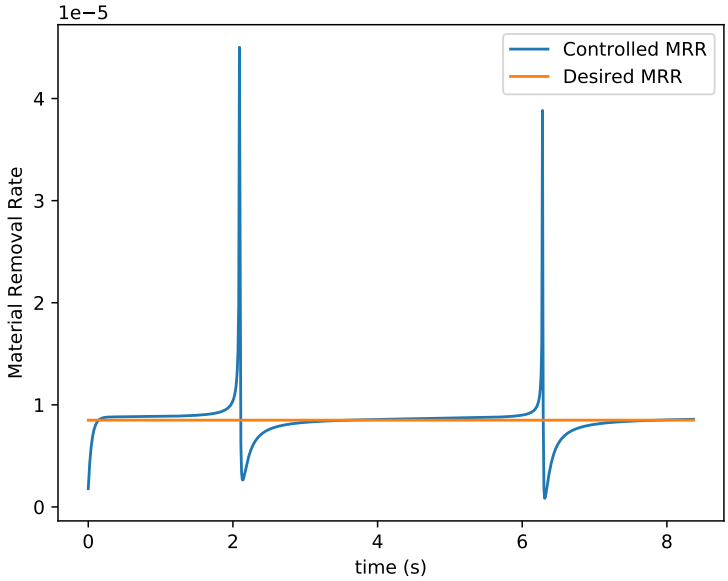

Figure 6.8: Desired and a simulation of the controlled material removal rate.

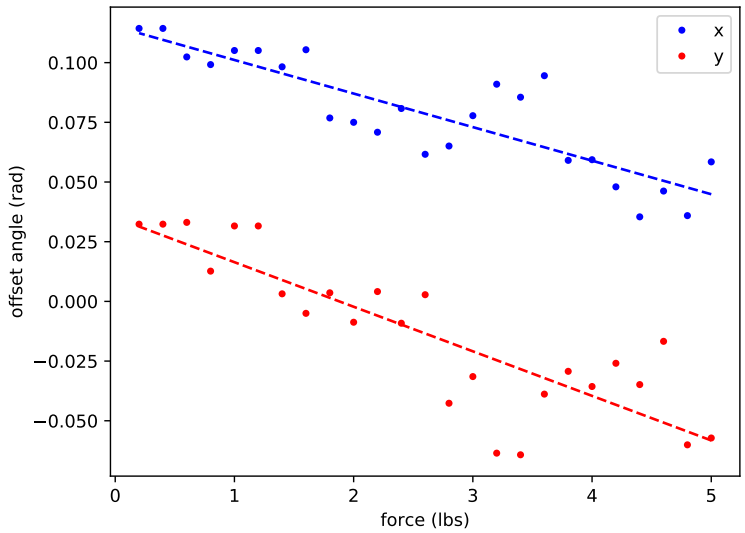

Figure 6.9: Manual sander normalization angle offsets vs applied force along with the respective linear fits.

Chapter 7

MATERIAL REMOVAL RATE CONTROLLER TEST

With a controller designed, an experiment was proposed and conducted to test the material removal rate controller on physical hardware. First, the test was simulated, then performed to ensure the results matched the theoretical outcome.

7.1 Simulated Material Removal Rate Test

To check the material removal rate controller produces a more even material removal rate, a simulation was run with the same parameters as in Sec. 6.2. In this simulation the material removed at all locations on the surface of a panel was determined. This simulation was run with both a constant force, and a constant material removal rate with results shown in Fig. 7.1 and 7.2 respectively. In the constant force simulation the endpoint of the travel where the sander linear velocity is zero are seen to be sanded more deeply. As expected, in the constant material removal rate simulation this problem is not present, however there is

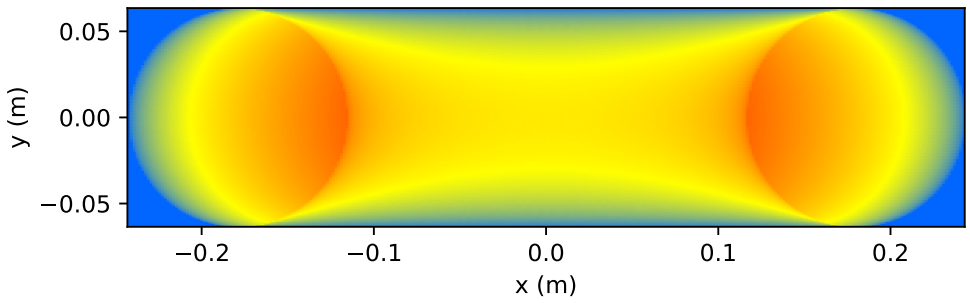

Figure 7.1: Material removed from sanding with a constant force with a linear path and sinusoidal position.

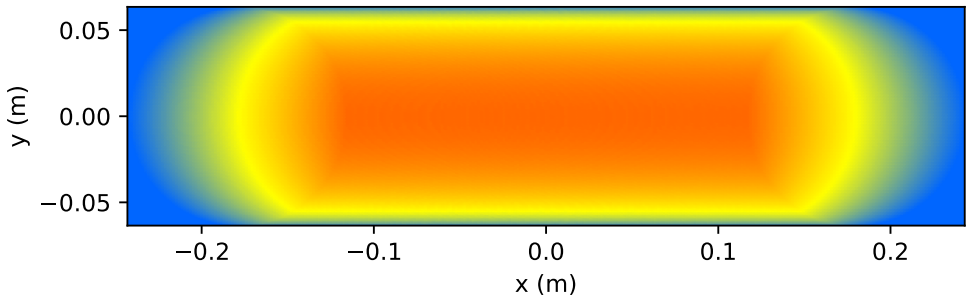

Figure 7.2: Material removed from sanding using the constant material removal rate controller with a linear path and sinusoidal position.

less sanding on the ends of the sander travel than ideal. These effects can more easily be seen in Fig. 7.3 which is the data from the center ($y = 0$) of the last two figures. The issue of less sanding happening at the ends of the sander travel is due to the sanding material removal rate model expecting the sander to travel its full diameter. This issue could be further mitigated if the entire path of the sander was known, but this would not be implementable for an operator controlled path, which this system uses.

7.2 Material Removal Rate Controller Test

Given the simulation in Sec. 7.1 the same test can be performed on the physical hardware. For this, test articles were created by 3D printing three different colored layers. This allows the amount of material removed to be seen visually. Two test articles were created and the two simulations in Sec. 7.1 were performed. However, the amplitude of the sanding had to be reduced because of the limited build volume of the 3D printer. The material removed under this smaller amplitude was simulated in Fig. 7.4 and 7.5. The results of these tests are shown in Fig. 7.6 and 7.7. From these images it can be seen that the normalization of the sander was not perfect. In general the results are still as expected, and somewhat match the simulations. For the constant force test in Fig. 7.6 it can be seen that more sanding does occur on the ends of the sander travel, as expected. There is also less sanding done in

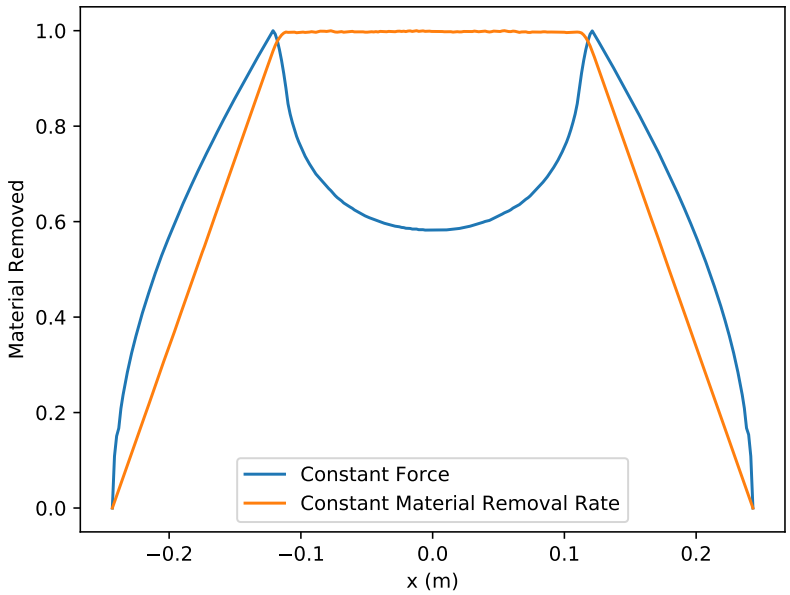

Figure 7.3: Normalized material removed from the center of the sander path ($y = 0$ in Fig. 7.1 and 7.2) with both constant material removal rate and constant force controllers with a linear path and sinusoidal position.

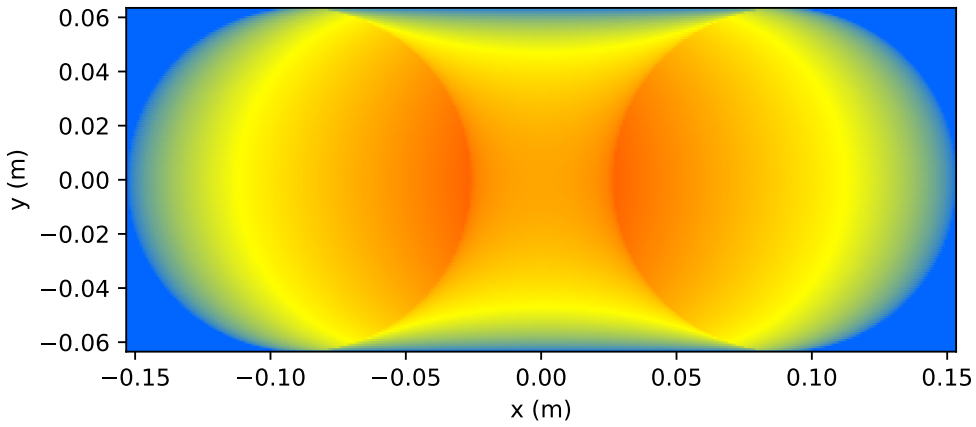

Figure 7.4: Material removed from sanding with a constant force with a linear path and sinusoidal position of the same amplitude as the physical experiment.

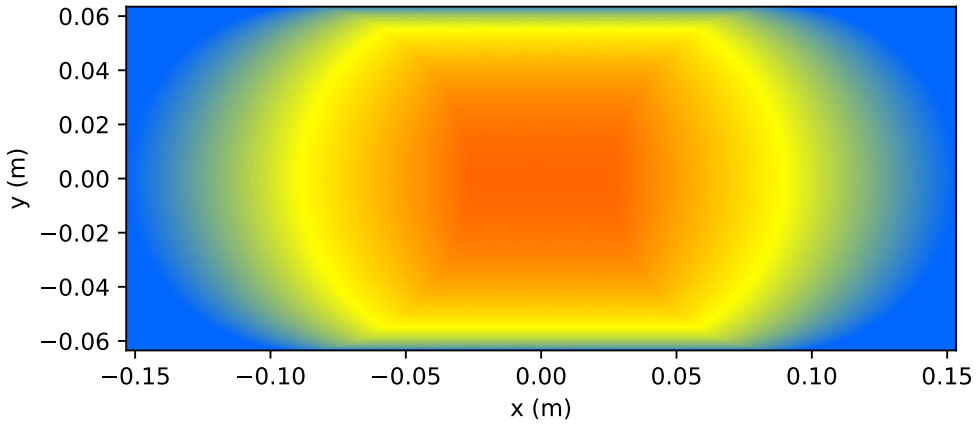

Figure 7.5: Material removed from sanding using the constant material removal rate controller with a linear path and sinusoidal position of the same amplitude as the physical experiment.

the very center of the sander travel due to the higher linear velocity of the sander. For the constant material removal rate test in Fig. 7.7, the sanding is mostly in the center area of the panel as in Fig. 7.7.

While this test was being performed the forces exerted were monitored, along with the calculated force required for a constant material removal rate. These forces are plotted in Fig. 7.8 where the desired force is f_{ref} and the measured forces is f in Fig. 6.6. The measured force was also smoothed using a moving average of the raw measured data. From this plot it can be seen that the controller implemented on the robot does a good job of tracking the desired force.

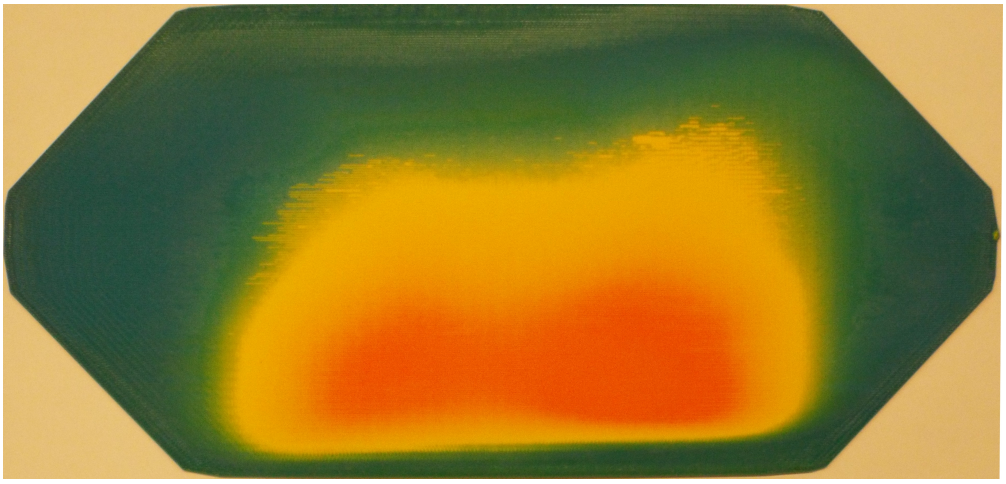

Figure 7.6: Heatmap of material removed due to sanding with a constant normal force.

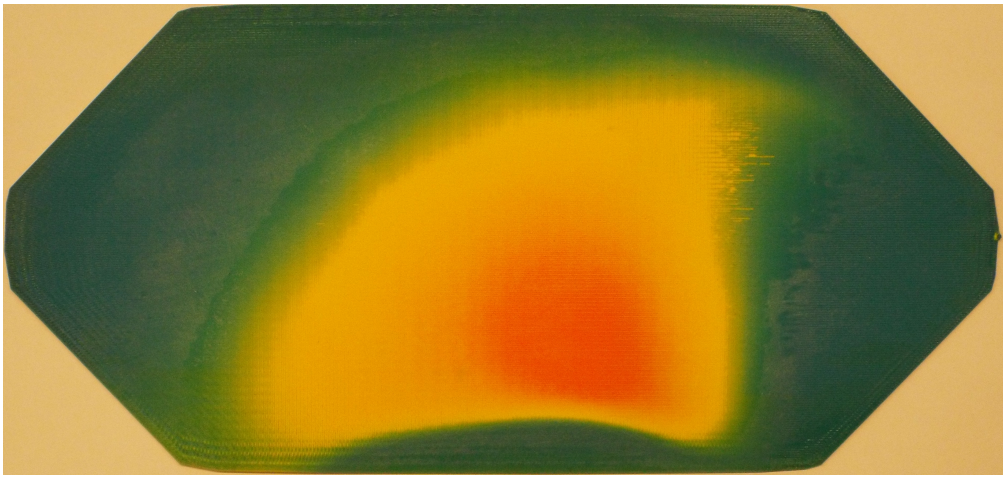

Figure 7.7: Heatmap of material removed due to sanding with a constant material removal rate as defined in Eq. 3.18.

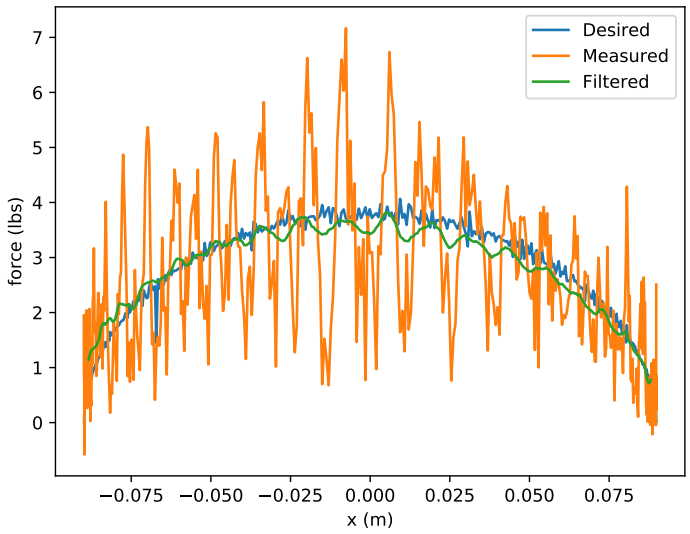

Figure 7.8: The desired and measured force from sanding with a constant material removal rate along with the measured force filtered using a moving average.

Chapter 8
CONCLUSION

The tests performed in Chapter 7 show that the model derived in Chapter 3 can be used to create a more evenly sanded workpiece. This is especially evident in Fig. 7.3. Although the physical tests performed in Chapter 7 are not a perfect match to the simulations in the same chapter, many of the same effects are visible. This shows the model of the material removal rate, and the controller, are working as expected. With a larger position amplitude, more of the effects seen in figures 7.1 and 7.2 could be observed. However, even with the relatively small amplitude tested, sufficient effects are visible to conclude that the tests were successful.

8.1 Future Work

The discrepancy between the simulations and the test results are primarily due to two factors: First, there is a large amount of slop in the robot. The Z-axis bearing of gantry has an especially low torsional stiffness around the x and y axes. This allows the sander to wander up to a half inch as it travels along the commanded path. Second, the series elastic actuators deflect when a load is applied to them, causing normalization errors which must be corrected.

To correct these issues the robot can be tuned, or modified if necessary, to minimize the flex in key components. A more advanced control system could also be designed, and implemented, to counteract deflections. However, replacing the custom robot with an off the shelf arm could be an effective, although more expensive, method of improving robot performance.

Replacing the robot would require some changes. Because the series elastic actuators are currently used to supply the necessary compliance to apply force to the workpiece, switching

to a robot with rigid joints would cause issues with force control. To fix this, an elastic element would have to be added. One advantage of this approach is the end effector could be designed with compliance only in the desired axes. The key direction being normal to the sander. This could create better positional accuracy while still allowing the force to be easily controlled.

To allow a larger position amplitude during tests, either a smaller sander, or a larger panel could be used. A test article could be constructed from multiple smaller panels to reach a sufficient size for the current sander. A sanding pad could also be modified to have a smaller diameter which would increase the effective stroke length.

Although this thesis only considered controlling the material removal rate for flat surfaces, there are many non-flat surfaces which require sanding. To allow this work to more broadly address the ergonometric concerns in Chapter 1, a model of the material removal rate for contoured surfaces is necessary. To effectively model the material removal rate on a contoured surface several more parameters must be know, most important of these is the local curvature of the surface. With this information, along with the compliance of the sanding pad, the contact area and pressure distribution can be determined. Using these quantities, the average material removal rate could be calculated.

BIBLIOGRAPHY

[1] Martin A. Fischler and Robert C. Bolles. Random sample consensus: A paradigm for model fitting with applications to image analysis and automated cartography. *Commun. ACM*, 24(6):381–395, June 1981.

[2] Gene F. Franklin, J. David Powell, and Michael L. Workman. *Digital Control of Dynamic Systems*. Addison Wesley Longman, Inc., 3 edition, 1998.

[3] Lennart Ljung. *System identification : theory for the user*. Prentice-Hall information and system sciences series. Prentice Hall PTR, Upper Saddle River, NJ, 2nd ed. edition, 1999.

[4] Parker Owan, Cameron Devine, and W. Tony Piaskowy. Corerobotics: An object-oriented c++ library with cross-language wrappers for cross-platform robot control. *The Journal of Open Source Software*, February 2018.

[5] Raphael Poiree, Sebastien Garnier, and Benoit Furet. Material removal distribution in roborobot random orbital sanding. *Research in Interactive Design*, 4:558–564, 2016.

[6] P. W. Preston. The theory and design of plate glass polishing machines. *Journal of the society of glass technology*, 1927.

[7] Derek Rowell and David N. Wormley. *System Dynamics: An Introduction*. Prentice Hall, 1997.

[8] Radu Bogdan Rusu. *Semantic 3D Object Maps for Everyday Manipulation in Human Living Environments*. PhD thesis, Computer Science department, Technische Universitaet Muenchen, Germany, October 2009.

[9] Radu Bogdan Rusu and Steve Cousins. 3d is here: Point cloud library (pcl). In *IEEE International Conference on Robotics and Automation (ICRA)*, Shanghai, China, May 9-13 2011.

Appendix A

MATERIAL REMOVAL RATE CONSTANT ESTIMATION TEST ORDER

1. Flat Panel with a max force of 6.0 lbs and a max velocity of 0.09 m/s.
2. Moose Nose Panel with a max force of 4.5 lbs and a max velocity of 0.135 m/s.
3. Sidewall Panel with a max force of 3.0 lbs and a max velocity of 0.09 m/s.
4. Flat Panel with a max force of 3.0 lbs and a max velocity of 0.09 m/s.
5. Moose Nose Panel with a max force of 3.0 lbs and a max velocity of 0.18 m/s.
6. Sidewall Panel with a max force of 4.5 lbs and a max velocity of 0.18 m/s.
7. Flat Panel with a max force of 4.5 lbs and a max velocity of 0.135 m/s.
8. Moose Nose Panel with a max force of 6.0 lbs and a max velocity of 0.135 m/s.
9. Sidewall Panel with a max force of 4.5 lbs and a max velocity of 0.135 m/s.
10. Flat Panel with a max force of 4.5 lbs and a max velocity of 0.18 m/s.
11. Moose Nose Panel with a max force of 3.0 lbs and a max velocity of 0.18 m/s.
12. Sidewall Panel with a max force of 3.0 lbs and a max velocity of 0.09 m/s.
13. Flat Panel with a max force of 4.5 lbs and a max velocity of 0.135 m/s.
14. Moose Nose Panel with a max force of 3.0 lbs and a max velocity of 0.09 m/s.
15. Sidewall Panel with a max force of 4.5 lbs and a max velocity of 0.09 m/s.
16. Flat Panel with a max force of 6.0 lbs and a max velocity of 0.135 m/s.
17. Moose Nose Panel with a max force of 4.5 lbs and a max velocity of 0.18 m/s.
18. Sidewall Panel with a max force of 3.0 lbs and a max velocity of 0.18 m/s.
19. Flat Panel with a max force of 3.0 lbs and a max velocity of 0.135 m/s.
20. Moose Nose Panel with a max force of 6.0 lbs and a max velocity of 0.09 m/s.
21. Sidewall Panel with a max force of 6.0 lbs and a max velocity of 0.18 m/s.
22. Flat Panel with a max force of 3.0 lbs and a max velocity of 0.18 m/s.

23. Moose Nose Panel with a max force of 6.0 lbs and a max velocity of 0.18 m/s.
24. Sidewall Panel with a max force of 6.0 lbs and a max velocity of 0.09 m/s.
25. Flat Panel with a max force of 4.5 lbs and a max velocity of 0.09 m/s.
26. Moose Nose Panel with a max force of 4.5 lbs and a max velocity of 0.09 m/s.
27. Sidewall Panel with a max force of 6.0 lbs and a max velocity of 0.18 m/s.
28. Flat Panel with a max force of 6.0 lbs and a max velocity of 0.18 m/s.
29. Moose Nose Panel with a max force of 3.0 lbs and a max velocity of 0.135 m/s.
30. Sidewall Panel with a max force of 3.0 lbs and a max velocity of 0.135 m/s.
31. Moose Nose Panel with a max force of 6.0 lbs and a max velocity of 0.09 m/s.
32. Sidewall Panel with a max force of 6.0 lbs and a max velocity of 0.135 m/s.